PAPER

Check for updates

Polystyrene nanoplastics as PFAS carriers and their interactions with zwitterionic phospholipid membranes

Jiahuiyu Fang,[a] Tongxuan Qiao,[b] Pranab Sarker,[ac] Xiaoxue Qin,[a] Size Zheng, [iD] [d] Mark J. Uline*[ac] and Tao Wei [iD] *[ac]

The co-occurrence of per- and polyfluoroalkyl substances (PFAS) and nanoplastics (NPs) poses a synergistic threat to environmental and human health, yet the molecular mechanisms governing PFAS–NP complexation and membrane interactions remain unclear. Using atomistic molecular dynamics simulations, we investigated the adsorption of neutral polytetrafluoroethylene (PTFE) and anionic perfluorinated compounds (perfluorooctanoic acid, PFOA, and perfluorooctanesulfonic acid, PFOS) on polystyrene NPs (3.1 and 6.7 nm) and their interactions with 1-palmitoyl-2-oleoyl-*sn*-glycero-3-phosphocholine (POPC) membranes. Polystyrene NPs act as carriers, transporting PFAS molecules to the lipid/water interface, where PFAS attachment modifies NP interfacial behavior. PFAS adsorption on the NP surface is driven by hydrophobic and fluorophilic interactions. Neutral PTFE exhibits inhomogeneous, partially penetrated adsorption, while anionic PFOS and PFOA form relatively homogeneous adsorption layers due to electrostatic repulsion among their anionic headgroups. In the POPC membrane, the exposed trimethylammonium groups with non−hydrogen-bonded water prevail over phosphate groups with hydrogen-bonded water, reducing the zwitterionic membrane's resistance to NP adsorption. Consequently, surface hydration hinders the attachment of neutral bare and PTFE-coated NPs, while anionic PFOS-coated NPs rapidly adsorb *via* electrostatic attraction to the positively charged POPC trimethylammonium groups, overcoming the hydration barrier. PFOA-coated NPs adsorb transiently; however, PFOA detachment exposes the NP core, weakening NP–lipid interactions and leading to NP desorption and insertion of detached PFOA molecules. The addition of 0.1 M KCl does not significantly alter the interfacial behavior of small PFAS–NP complexes.

Introduction

Per- and polyfluoroalkyl substances (PFAS)—often referred to as "forever chemicals"—have emerged as contaminants of growing global concern due to their widespread presence and extreme persistence in the environment.[1,2] Resistant to degradation,[1,3,4] PFAS are routinely detected across various environmental media,[5] particularly in aquatic ecosystems and even in drinking water supplies.[6,7] More alarmingly, these substances can bioaccumulate across trophic levels,[8–12] from phytoplankton and fish to marine mammals and terrestrial wildlife, resulting in pervasive ecological exposure. A growing body of scientific evidence has linked PFAS to a range of serious health effects, including cancer, cardiovascular and respiratory diseases,

neurological disorders, and suppression of the immune system.[13] Anionic perfluorooctanoic acid (PFOA) and perfluorooctanesulfonic acid (PFOS), which contain hydrophobic fluorocarbon chains and charged headgroups, are among the most pervasive PFAS in aquatic environments.[14] Their amphiphilic structures, combining hydrophobic and lipophilic fluorocarbon backbones with charged headgroups, enhance mobility in water and promote adsorption onto solid surfaces.

Microplastics (MPs, 1 μm–5 mm) and nanoplastics (NPs, <1 μm) are small fragments of synthetic polymers originating from the degradation of larger plastic debris through physical, mechanical, or biological weathering, or from direct manufacturing.[15–18] They enter ecosystems directly through industrial products, such as abrasive microbeads in personal care items and synthetic fibers released from textiles during washing.[19–22] These particles are now ubiquitous in aquatic and terrestrial environments, where they pose significant risks to both wildlife and human health.[22–24] The dominant transmembrane transport mechanism (such as, passive diffusion *vs.* active endocytosis) of MPs and NPs depends on particle

[a]*Department of Biomedical Engineering, University of South Carolina, Columbia 29208, SC, USA. E-mail: ULINE@cec.sc.edu; taow@mailbox.sc.edu*

[b]*Syosset High School, Syosset, New York 11791, USA*

[c]*Department of Chemical Engineering, University of South Carolina, Columbia 29208, SC, USA*

[d]*Department of Chemistry, Stony Brook University, Stony Brook, New York 11794, USA*

properties such as surface hydrophobicity, charge, size, and shape, as well as the characteristics of the cellular environment.[25–27] Similar to PFAS, NPs are toxic and resistant to biodegradation. Due to their smaller size, NPs more readily penetrate biological membranes and exert stronger toxicological effects than MPs.[25,26,28,29]

MPs and NPs can adsorb various pollutants, heavy metals, and organic macromolecules that coexist in the environment.[30] Recent experiments[8,31–36] showed that MPs and NPs can adsorb PFAS, forming combined pollutant complexes with synergistic effects. The adsorption of PFAS with MPs or NPs can alter PFAS partitioning in the aqueous environment.[35] Due to the large specific surface area of MPs/NPs and their strong hydrophobic interactions with PFOA,[37] they can facilitate the transport and dispersion of PFAS across ecosystems, contributing to secondary pollution pathways and broader environmental dissemination.[32,35,38] High PFAS concentrations on MPs (1.05–9.07 × 10³ ng g⁻¹) were detected in drain outlets receiving wastewater from highly urbanized cities.[36] PFOS and PFOA were identified as the most abundant compounds adsorbed onto the MPs, with the proportion of PFOS being higher than that of PFOA.[36] The formation of such complexes can amplify both environmental persistence and biological toxicity.[32,33] Consequently, their combined presence can lead to more severe adverse effects on aquatic organisms, wildlife, and potentially human health, including intensified toxicity, bioaccumulation, and disruption of physiological systems.[32,39,40] Understanding the combined impact of co-occurring microplastics and PFAS is therefore crucial for advancing environmental risk assessments and guiding effective mitigation strategies.

Molecular dynamics (MD) simulations have been extensively applied to study the interfacial behaviors of various materials, such as lipids, polymers and nanoparticles at the atomistic and molecular coarse-grained scales, revealing structures with atomistic resolution and dynamics over picosecond to microsecond timescales.[41–60] Recent atomistic MD simulations[41,61] showed that PFAS molecules can easily insert into phospholipid bilayers, driven by the free energy gradient between bulk water and the lipid membrane. On the zwitterionic phospholipid surface, electrostatic interactions between positively charged trimethylammonium groups of phospholipids and anionic PFAS molecules such as PFOA, PFOS, and perfluorobutanoic acid (PFBA) initially attract PFAS to the membrane, and hydrophobic interactions between their fluorocarbon tails and lipid chains subsequently drive their reorientation and insertion.[41] Consistently, other recent MD simulations[62] showed that the strong adsorption of PFOA and PFOS on montmorillonite is primarily governed by electrostatic interactions between their oxygenated and sulfonate functional groups and the negatively charged clay surfaces. In contrast, the adsorption of PFOA, PFOS, and fluorotelomer alcohol on polyethylene and polypropylene polymer surfaces is dominated by hydrophobic interactions of their fluorocarbon tails with the polymer surfaces.[62] On the pyrophyllite surface, adsorbed PFASs strongly prefer to form a monolayer, in which PFOS molecules adopt specific orientations relative to one another (aligning either parallel or antiparallel), while PFOA molecules adsorb

disorderly at the interface.[42] Recent MD simulations showed that the elastic deformation of a POPC (1-palmitoyl-2-oleoyl-*sn*-glycero*-3-phosphoscholine) membrane hinders the penetration of charge-neutral semicrystalline polyethylene NPs through the lipid membrane *via* passive diffusion.[50] It was also found that negatively charged polystyrene (PS) NPs can adsorb onto the POPC membrane surface.[51]

Despite extensive previous experimental efforts,[8,31–35] the molecular interactions between PFAS molecules and NPs are not fully understood. The interfacial behavior of PFAS–NP complexes on phospholipid membranes also remains unknown. To address this knowledge gap, we employed atomistic MD simulations to investigate the adsorption of PFAS molecules on PS-NPs and the interactions of PFAS-coated NPs with the surface of POPC lipids, a major component of cell membranes in the human body. We examined PFAS molecules with various functional groups in the bulk water, including neutral polytetrafluoroethylene (PTFE) and the anionic PFOS and PFOA (Fig. 1). To evaluate the size effects on PFAS adsorption, PS-NPs with diameters of 6.7 nm and 3.1 nm were studied. Moreover, we compared the interfacial behaviors of PS-NPs coated with anionic PFOA and PFOS, as well as neutral PTFE, in pure water and in a 0.1 M KCl solution. This work provides important insights into the interactions and migration of PFAS and NPs in aqueous environments, which are essential for developing effective strategies for environmental remediation. It also yields valuable insights into the attachment of PFAS–NP colloids on phospholipid membrane surfaces, which represents a critical initial step in passive diffusion and the biological process of endocytosis.

Computational details

The atomistic MD simulations were performed using the GROMACS software (version 2019.6).[63] The CHARMM36 force field[64] was used for PS NPs, and the CHARMM TIP3P water model[65] was applied with the structures constrained using the SETTLE algorithm.[66] Parameters of PFAS bonded interactions (bonding, angle, dihedral, and improper dihedral) were taken
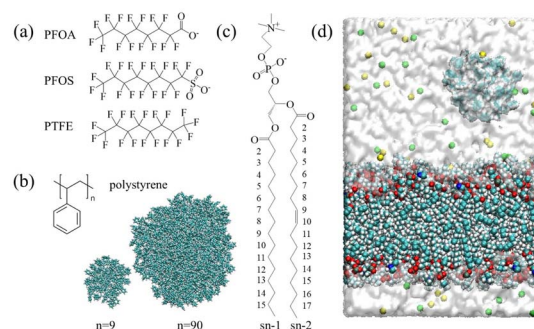

Fig. 1 (a) Molecular structures of PFAS molecules. (b) Snapshot of 3.1 nm (left) and 6.7 nm (right) amorphous PS NP, with C and H atoms in cyan and white. (c) Molecular structure of a POPC molecule. (d) Snapshot of POPC membrane (O: red; N: blue; P: tan; H: white). Note: a POPC molecule contains 2 fatty acid chains attached at the stereospecific numbering 1 and 2 (sn-1 and sn-2).

from the literature,[67] and partial charges were obtained *via* quantum computation of density functional theory (DFT) using the restrained electrostatic potential (RESP) method established in our previous paper.[41]

Two PS-NPs with diameters of approximately 6.7 nm and 3.1 nm, respectively, were assembled using the atactic configuration of PS chains generated from the CHARMM-GUI web server.[68] The large NP (6.7 nm) contained 10 PS chains with a degree of polymerization (DP) of 90, and the small NP (3.1 nm) contained 10 PS chains with a DP of 9. Extended polymer chains were relaxed in vacuum for 100 ns through heating and annealing at 298–500 K, forming globular NPs. Each PS NP was then solvated in a cubic water box and equilibrated for 100 ns.

To model PFAS adsorption at dilute concentrations (∼0.02 M) in a small solvation box, a refilling procedure was employed (Fig. 2). Twenty and four PFAS chains were sequentially added to the large and small NP systems, respectively, with Na^+ counterions included for PFOA and PFOS. Each system was equilibrated for 100 ns after each addition, repeated ten times. For the large NP systems, a fraction of PFOA and PFOS molecules remained in the bulk phase after ten refilling steps, indicating maximum adsorption. In contrast, all PFAS molecules adsorbed onto the small NP surfaces, suggesting that adsorption in those systems had not yet reached saturation. To validate PTFE adsorption, two additional refilling steps were performed; however, all newly added PTFE molecules adsorbed onto the NP surfaces. Due to the high computational cost, further refilling was not attempted on the small NPs. During the final refilling, the systems were further relaxed for 1 μs (PFOA/PFOS), 2 μs (PTFE on the large NP), and 400 ns (PFAS on the small NP) to examine the coating morphologies.

A POPC lipid bilayer, a major component of cell membranes (Fig. 1d), was constructed with 238 POPC molecules in an 8.67 × 8.67 × 13 nm³ box using CHARMM-GUI.[68] Two systems (pure water and 0.1 M KCl) were prepared to assess ionic effects, each containing either bare NPs of different sizes or PFAS–NP complexes. Pure lipid membranes were first equilibrated in the Isothermal–isobaric ensemble (*NPT*) ensemble for 150 ns to ensure full relaxation. Bare or PFAS-coated NPs were then positioned ∼1.0 nm from the membrane to enable spontaneous adsorption. Simulations were run in the *NPT* ensemble for over 200 ns using a 1.0 fs time step. Temperature (298.15 K) was maintained with a velocity-rescale thermostat, and pressure (∼1 atm) with a Parrinello–Rahman barostat.[69] Periodic boundary conditions (PBC) were applied in all simulations of this work.
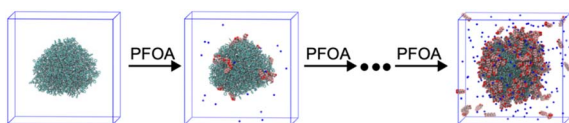

Fig. 2 Simulation process of the gradual adsorption of PFAS onto the large PS NP. In each step, 20 PFOA chains (with Na^+ counterions) were added, repeated 10 times until 200 PFOA chains were present. Each intermediate step ran for 100 ns, and the final equilibrium step ran for 400 ns. Water is omitted for clarity. Carbon, fluorine, oxygen, hydrogen, and sodium ions are colored cyan, orange, red, white, and blue, respectively.

Results and discussion

As illustrated above, after refilling the system ten times with anionic PFOA or PFOS, the maximum adsorption amount on the large NP surface (6.7 nm) is achieved (Fig. S1a and b in the SI). In contrast, all PTFE molecules adsorb completely, with none remaining in solution (Fig. S1c, SI), suggesting a nonequilibrium segregation of fluorinated groups within the adsorbed PTFE layer. On the 6.7-nm PS-NP surface, the mass ratio of the adsorption amount of PFOA and PFOS to the NP is 0.78 and 1.03, respectively. For the PTFE adsorption, this ratio can exceed 1.12, as adsorption has not yet reached equilibrium (Table S1 in the SI). The large surface area of NPs greatly increases the adsorption of PFAS molecules. The adsorption behavior of PFOA and PFOS in our study is consistent with previous experimental reports,[35] which showed that their adsorption can reach equilibrium partition. However, distinct adsorption morphologies are observed for different types of PFAS. PFOA and PFOS molecules adsorb on the NP surface comparatively homogeneously, whereas PTFE exhibits pronounced segregation (Fig. 3a and S2 in the SI). The initial adsorption is driven by the strong hydrophobic interactions between the PS-NP and the PFAS fluorocarbon chains, as evidenced by the dominant Lennard-Jones (LJ) attraction between PFAS and the NPs (Fig. S3 in the SI). The fluorophilic interaction[70] drives the subsequent self-segregation of fluorinated groups, as PTFE molecules prefer to associate with one another rather than distribute uniformly across the PS-NP surface. Conversely, electrostatic repulsion between their anionic head groups (carboxylate ion ($-CO_2^-$) for PFOA and sulfonate ion ($-SO_3^-$) for PFOS) leads to a more homogeneous distribution on the NP surface by preventing molecular aggregation. As shown in Fig. 3b, the density distribution as a function of distance from the NP center indicates that the hydrophobic fluorocarbon chains of PFOA and PFOS preferentially orient toward the NP interior, while their anionic head groups remain exposed to water on the NP surface (Fig. 3a, bottom). In contrast, PTFE molecules tend to segregate on the NP surface, with some also penetrating into the NP after entering the NP hydrophobic core (Fig. 3a). Our results are consistent with a previous simulation study,[71] which showed that hydrophobic interactions of fluorocarbons play a dominant role in PFAS adsorption on the graphene surface.

We further examined the adsorption of PFOA, PFOS, and PTFE on the small PS NP (3.1 nm) to assess the effect of NP size. No significant size-dependent influence was observed on the adsorption homogeneity of the PFAS molecules. Similar to the large NP (6.7 nm), the negatively charged PFASs (PFOA and PFOS) exhibit relatively homogeneous adsorption, whereas the charge-neutral PTFE shows inhomogeneous adsorption (Fig. 4a, top). Consistent with the large NP, on the small NP, the anionic headgroups ($-CO_2^-$ for PFOA and $-SO_3^-$ for PFOS) remain exposed to water, while the hydrophobic fluorocarbon tails orient toward the NP interior with deeper penetration, as indicated by the positions and extents of the density profiles in Fig. 4b. Similar to Fig. 3b, the density peaks of the head and tail
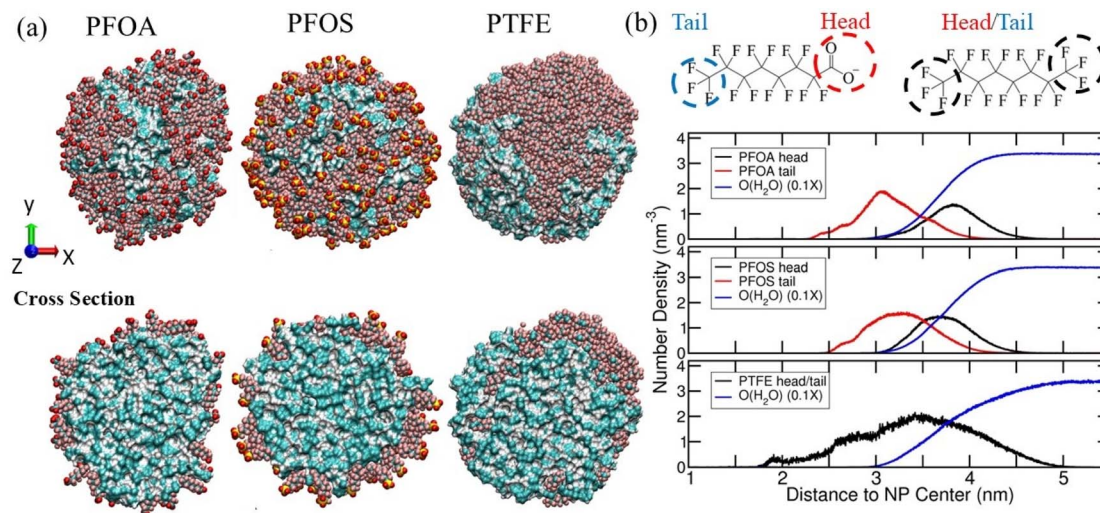
Fig. 3 (a) Adsorption of PFOA, PFOS, and PTFE on the 6.7-nm polystyrene NP surface: (top) the overall molecular aggregates and (bottom) corresponding cross-sectional views. (b) Density distribution of headgroups ($-CO_2^-$ for PFOA and $-SO_3^-$ for PFOS), tail ($-CF_3$) groups, and water oxygen atoms. Ten and twelve refilling steps plus an additional 1.0 μs relaxation were applied to generate PFOA-/PFOS- and PTFE-coated NPs, respectively.

groups are located on opposite sides of the NP surface near the NP core. However, for the smaller NP, PTFE molecules tend to segregate both on the NP surface and within the NP after penetrating its hydrophobic core (Fig. 4a, bottom). The internal segregation is further supported by the density profile (Fig. 4b), which exhibits pronounced peaks near the NP center. This again demonstrates the fluorophilic interaction and fluoro-phobic effect.[70]

The orientation of PFAS molecules can be further analyzed based on their relative orientations with respect to the NP's radial vector. To quantify their anisotropic orientation, we used

the second-order Legendre polynomial orientational function[41,72]

$$O(r) = \frac{1}{N(r)} \sum \left[\frac{3\cos^2\theta(r) - 1}{2} \right] \qquad (1)$$

where $N(r)$ is the total number at r and $\theta(r)$ is the angle between two vectors (Fig. 5a): one pointing from the NP center of mass (COM) to a terminal C atom of a PFAS molecule and the other connecting this terminal C atom to the opposite terminal C atom. The orientational function $O(r)$ ranges from -0.5 to 1.0 for $0° \leq \theta \leq 90°$. When $O(r) = -0.5$ ($\theta = 90°$), a PFAS molecule tends to adopt an orientation of lying down on the surface.
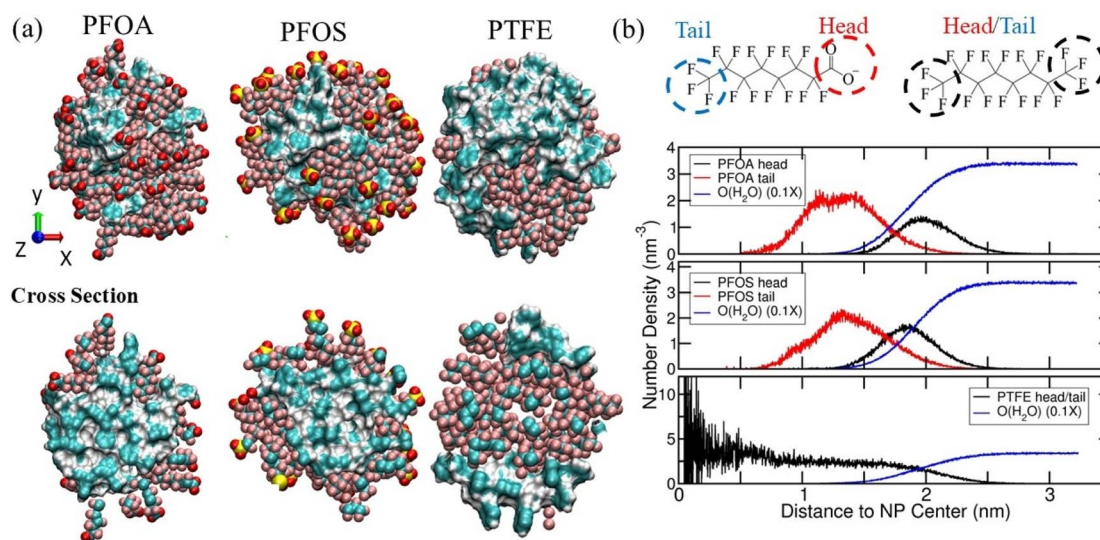
Fig. 4 (a) Adsorption of PFOA, PFOS, and PTFE on the 3.1-nm polystyrene NP surface: (top) the overall molecular aggregates and (bottom) corresponding cross-sectional views. (b) Density distribution of headgroups ($-CO_2^-$ for PFOA and $-SO_3^-$ for PFOS), tail ($-CF_3$) groups, and water oxygen atoms. Ten refilling steps, followed by an additional 400 ns relaxation, were applied to generate all the complexes.
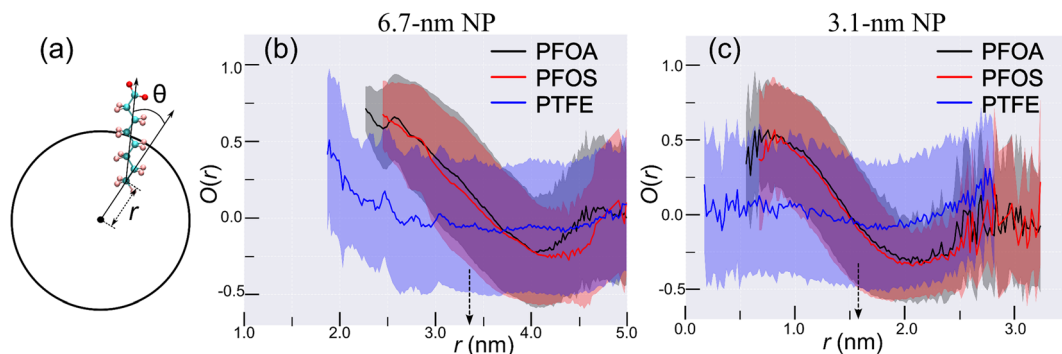
Fig. 5 Orientation of PFAS chains: (a) angle defining the relative orientation between the NP radial vector and a PFAS chain vector; (b) 6.7-nm NP; and (c) 3.1-nm NP. In all calculations, the entire trajectory was used. The arrows denote the location of the NP surface.

When $O(r) = 1$ ($\theta = 0°$), the molecule adopts a stand-up orientation, inserting its hydrophobic fluorocarbon tail group into the PS NP while directing its charged headgroup ($-CO_2^-$ for PFOA and $-SO_3^-$ for PFOS) toward water. When $O(r) = 0$, PFAS molecules exhibit no preferred orientation.

As shown in Fig. 5b and c, the values of $O(r)$ for PFOA and PFOS tend to be positive inside the NP surface and predominantly negative on top of the NP surface. This suggests that, irrespective of NP's size, the PFOA and PFOS chains favor a stand-up orientation to a greater extent when located in the NP interior, while preferably lying down when distributed on the NP surface. In contrast, PTFE molecules display anisotropic orientational behavior that depends on the NP size. For the smaller NP, the $O(r)$ values of PTFE are nearly zero inside the NP surface, indicating no distinct orientational preference. By contrast, for the larger NP, PTFE molecules exhibit a weaker but still noticeable stand-up orientation inside the NP.

Hydration and spatial distribution of POPC lipid membrane

To study the interactions of NPs with the POPC lipid membrane, we first equilibrated the POPC bilayers in pure water for more than 150 ns. The surface hydration of the lipid layers was analyzed using the proximal radial distribution function,[73,74] $pG(r) = \rho(r)/\rho_{bulk}$, which represents the ratio of the local water density $\rho(r)$ to the bulk water density ρ_{bulk}, with r being the shortest distance between a water oxygen atom and lipid membrane atoms. As shown in Fig. 6a, a condensed hydration peak is observed at approximately 0.3 nm above the lipid surface, which demonstrates that the lipid layer surface is covered by a condensed hydration water layer that provides a hydration barrier for the biofoulers' attachment. To characterize the distribution and ordering of these interfacial water molecules, two-dimensional water distribution ($\omega(Z,\theta)$)[73–75] was adopted.

$$\omega(Z, \theta) = \frac{\langle \delta(\theta - \theta(t))\delta(Z - Z(t))\rangle}{\omega_0 \rho(Z)\ \sin\theta} \quad (2)$$

where θ represents an angle between the dipole vector of a water molecule and the Z-axis, $\rho(Z)$ is the local water density at Z, $\sin(\theta)$ is the angular Jacobian factor, and ω_0 is the averaged bulk

value of orientational distribution for normalization. As shown in Fig. 6b, a hotspot appears above the POPC surface at 1.9 nm $\leq Z \leq 2.0$ nm and $0° \leq \theta \leq 30°$. This indicates that a higher population of water molecules has orientational preference driven by the interaction between zwitterionic POPC and surrounding water molecules.

Fig. 6c presents the density profiles of nitrogen and phosphorus atoms in lipids along the Z-axis, corresponding to positively charged trimethylammonium ($-N^+(CH_3)_3$) and negatively charged phosphate ($-PO_4^-$) groups, respectively (Fig. 6a). The trimethylammonium groups occupy the outermost lipid surface, whereas the phosphate groups lie slightly beneath. The oxygen atoms of POPC lipids (from phosphate and ester linkages; see POPC molecular structure in Fig. 1) show a density peak at $Z \approx 1.7$ nm (Fig. 6c), displaced by approximately 0.2–0.3 nm from the region of maximum water density (Fig. 6b). This shift indicates hydrogen bonding between lipid oxygens and water hydrogens.

However, such a membrane structure, with the phosphate groups partially buried within the lipid surface, limits hydrogen bonding between the oxygen atoms of the phosphate and ester groups in POPC lipids and the hydrogen atoms of bulk water, thereby compromising the surface resistance to anionic PFAS-coated NPs, as discussed below. The number of hydrogen bonds between POPC lipids and water molecules was calculated using a geometric criterion, in which the distance between the donor (D) and acceptor (A), $d \leq 3.0$ Å, and the donor–hydrogen–acceptor (D–H$\cdots A$) angle satisfies $\theta \geq 150°$. Approximately 42% of the water molecules act as hydrogen-bond donors to the oxygen atoms of phosphate, ether, and carbonyl groups on the POPC lipid membrane surface within the first hydration shell ($r \leq 3.3$ Å). These interfacial hydrogen-bonding interactions give rise to a preferred orientation of water dipole vectors at the lipid–water interface (Fig. 6c). This finding suggests that, in addition to hydrogen-bonded water, the POPC membrane surface is also covered by a substantial fraction of non–hydrogen-bonded water molecules (58% of the total in the first hydration shell up to the hydration peak), which exhibit relatively weaker interactions with the surface. The ratio of hydrogen-bonded water molecules to oxygen atoms in the phosphate groups ($-PO_4^-$) is only about 0.32. This indicates that
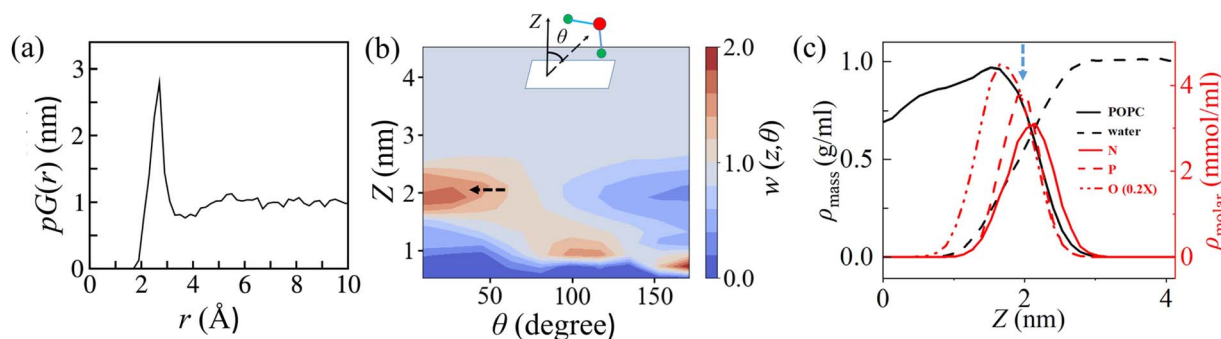
Fig. 6 Hydration profile and component distribution of a pure POPC lipid membrane in water without NPs: (a) proximal radial distribution function $pG(r)$; (b) two-dimensional orientational distribution $\omega(Z, \theta)$ of water at the POPC–water interface as functions of the Z-coordinate and θ; (c) density distribution $\rho(Z)$ along the Z-axis for POPC lipids, water, and atoms of POPC lipids (N, P, and O atoms). The black arrow in (b) indicates the hotspot corresponding to the region of a higher water density, and the blue arrow marks the peak of the high oxygen density region. Note: in (b) and (c), the symmetric center of the bilayer is taken as the origin of the Z-axis. Due to the symmetric structure of the lipid bilayer, the density profiles of the upper lipid leaflet are shown starting from the bilayer's symmetry center. For clarity, the O-atom density is scaled by a factor of 0.2 in (c).

the spatial distribution—where the positively charged tri-methylammonium groups are located on top of the POPC lipid surface and the negatively charged phosphate groups are situated underneath—is not conducive to the formation of the maximum number of hydrogen bonds with interfacial water, thereby limiting the membrane's fouling resistance. As shown in our previous studies, for polymer-brush surfaces terminated with zwitterionic trimethylamine N-oxide (TMAO)[74,76] and carboxybetaine (CBAA) groups,[73] most negatively charged oxygen sites are exposed on the polymer surface, forming strong hydrogen bonds with surface water molecules and establishing a robust hydration barrier against biofouling. Notably, the observation here that more positively charged tri-methylammonium groups are exposed to the bulk water is consistent with our previous study,[41] which demonstrated that the electrostatic potential increases across the POPC–water interface, hence promoting the insertion of anionic PFOA and PFOS molecules into the POPC lipid layers.

Interactions of PFAS-polystyrene nanoplastic complex with POPC lipid membrane

To investigate the interactions between the PFAS–NP complex and the POPC lipid membrane, we placed the bare NPs of different sizes, as well as the complex near the lipid bilayer surface in pure water. The minimum distance between the NPs and the membrane, as well as the corresponding interaction energies (electrostatic and LJ contributions), were monitored. Fig. 7 shows the adsorption behavior of bare 3.1-nm NPs and PTFE-coated NPs on the POPC membrane surface and their interactions. It was observed that the small NP repeatedly approaches the membrane surface (~0.2 nm) and is subsequently rebounded away over the course of 160 ns of simulation (Fig. 7a, bottom). The energy profile indicates that adsorption is primarily driven by weak LJ interactions (i.e., hydrophobic interactions between PFAS fluorocarbons and lipid hydrocarbons), with a maximum attractive energy of approximately −75 kJ mol⁻¹ (Fig. 7a, top). In contrast, electrostatic

interactions exert a small repulsive effect, reaching up to ~20 kJ mol⁻¹. The weak NP–lipid interactions make it difficult for small NPs to overcome the hydration energy barrier at the lipid surface and attach to the membrane within our simulation timescale of 160 ns. Our result is consistent with a previous atomistic MD study,[77] which showed that small PS NPs do not adsorb onto the POPC lipid surface within 500 ns. Another atomistic MD simulation also showed that, for small bare PS NPs with a diameter of 4.0–4.5 nm, the free energy barrier of POPC lipid hydration is 33.9 ± 8.9 kJ mol⁻¹,[78] which, although not significantly larger than the thermal energy, substantially increases the adsorption time.

To study the effect of NP size on adsorption, we increased the NP diameter from 3.1 to 6.7 nm. The larger NP remained bound to the lipid membrane for a longer period before desorption, rather than rapidly rebounding like the smaller 3.1 nm NP, due to stronger NP–lipid membrane LJ interactions (Fig. S4 in the SI). However, these interactions are still not sufficiently strong to overcome the Brownian thermal force and the hydration barrier of the POPC membrane. Our results are consistent with a previous simulation study,[50] which demonstrated that the POPC membrane resists the penetration of a bare polyethylene NP into the lipid membrane surface via passive diffusion due to the large elastic energy associated with lipid membrane deformation. Notably, large-scale CG MD simulations showed that a large bare PS NP (5–10 nm) can adsorb onto the lipid surface and translocate across the lipid membrane over a longer time-scale,[79] although they have lower resolution and cannot represent lipid surface hydration as precisely as atomistic MD simulations, which limits the accurate representation of microdynamic timescales. Despite the shorter time scale accessible to our atomistic simulations, our results highlight the critical role of the hydration barrier arising from the zwitterionic phosphorylcholine headgroups of POPC during NP attachment, which prolongs NP adsorption. Moreover, our study demonstrates that increasing NP size enhances NP–lipid surface interactions, thereby promoting NP adsorption. Like the
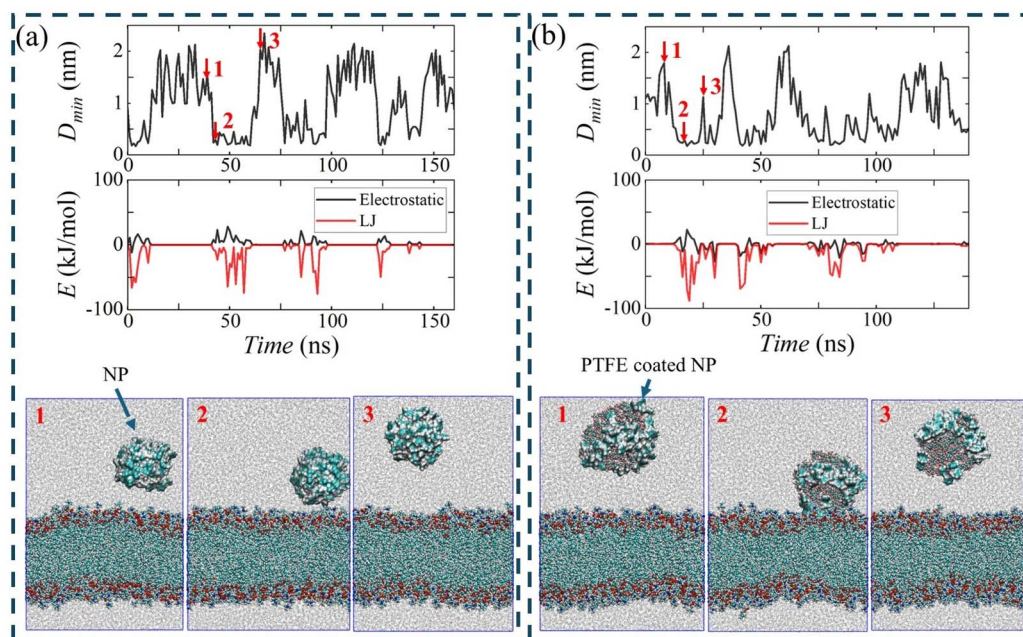
Fig. 7 Minimum distance D_{min} and interaction energies E (LJ and electrostatic) between the POPC membrane and (a) bare 3.1-nm NP and (b) PTFE-coated 3.1-nm NP in pure water as a function of simulation time t, along with the representative snapshots.

bare NPs, the small (3.1 nm) NP coated with PTFE repeatedly lands on and rebounds from the POPC membrane surface, driven mainly by weak LJ interactions, *i.e.*, hydrophobic interactions ($\sim$−90 kJ·mol^{-1}) over 140 ns of simulation (Fig. 7b). When the ion concentration is increased to 0.1 M KCl, no visible changes are observed in the interfacial behavior of either NP (Fig. S5 in the SI); neither the bare nor the PTFE-coated NP attaches to the POPC lipid membrane surface.

Unlike the charge-neutral bare and PTFE-coated NPs, the small NP coated with anionic PFOS exhibits rapid adsorption from bulk water and remains stably attached to the POPC lipid surface throughout the 260 ns simulation (Fig. 8a). To confirm the reproducibility of this behavior, three independent simulations with different initial configurations and velocities were performed. All of them show that PFOS-coated NPs adsorb rapidly and stably onto the POPC surface. The negatively charged –SO$_3^-$ group of PFOS interacts electrostatically with the positively charged –N$^+$(CH$_3$)$_3$ group of POPC (Fig. 8b), thereby promoting adsorption. Compared with the pure POPC surface, the adsorption of a PFOS-coated NP leads to a reduction of up to approximately 10–14 hydrogen bonds between the POPC surface and bulk water. This indicates that interfacial hydration water, particularly interfacial hydrogen-bonded water, presents a barrier to NP adsorption. Interaction energy analyses show that adsorption is dominated by electrostatic interactions, with a strong attractive energy of −558.86 kJ mol^{-1}, whereas the LJ contribution is relatively modest at −226.75 kJ mol^{-1} (Table 1). Typically, the electrostatic attraction between the –SO$_3^-$ group of PFOS and the –N$^+$(CH$_3$)$_3$ group of POPC plays a key role (Fig. S6 in the SI). It is also notable that most PFOS molecules remain stably bound to the NP surface, except for three molecules that detach (Table S1 in the SI and Fig. 8b). After diffusing

into the bulk water, the detached PFOS molecules subsequently insert into the lipid membrane surface, consistent with our previous study[41] on PFAS insertion into POPC lipid layers (Fig. 8b). Our findings are also in agreement with the recent experiments,[26] which showed that the negatively charged PS-NPs of 50 nm and 500 nm can be internalized into living cells through both passive membrane penetration and active endocytosis.

To study the effect of electrolytes on the anionic PFOS-coated NP adsorption on the lipid surface, an additional simulation was conducted for the system containing the small NP in the 0.1 KCl solution. Adsorption of the PFOS-coated NP also occurs (Fig. S7 in the SI) and remains stable thereafter. Similar to the adsorption in pure water, electrostatic attractions are stronger than the LJ interactions (Table 1). Likewise, the interactions of the –SO$_3^-$ group of PFOS on the NP surface and the –N$^+$(CH$_3$)$_3$ group of POPC lipids is also critical for the PFOS-coated NP adsorption on the lipids (Fig. S8 in the SI). These results suggest that the presence of K$^+$ and Cl$^-$ ions at 0.1 M does not discernibly affect the adsorption kinetics of anionic PFOS-coated NP onto the POPC lipid membrane surfaces. The total interaction energies between the PFOS-coated NP and the POPC lipid membrane in pure water and in 0.1 M KCl solution are comparable (Table 1). The slight difference may arise from variations in the adsorption sites and local morphologies of the PFOS-coated NP surface.

For the anionic PFOA-coated NP system, it was found that although the complex remains adsorbed on the POPC membrane for an extended period (over 100 ns), this adsorption is unstable and eventually leads to desorption. During this adsorption/desorption process, PFOA molecules on the NP surface are unstable, continuously detaching from and

Paper
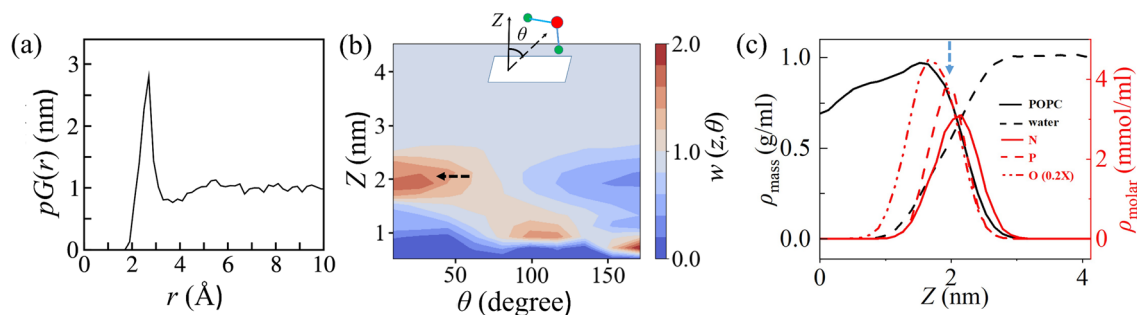
Fig. 8 Adsorption of PFOS-coated NPs on the POPC lipid membrane surface in pure water. (a) Minimum distance D_{min} between the POPC membrane and the PFOS-coated NP as a function of simulation time t. (b) Snapshots of the PFOS-coated NPs adsorbed on the POPC lipid surface, along with a zoomed-in view of the adsorbed PFOS molecules and the corresponding POPC surface. Water molecules are omitted for clarity. Atoms in the system are shown as pink (F), cyan (C), green (C), yellow (S), red (O), blue (N), white (H), and tan (P). Note: due to the PBC along the Z-axis in our simulations, PFOS can adsorb onto both the upper and lower lipid leaflets.

Table 1 Interaction energies (electrostatics (E_{elect}) and LJ (E_{LJ})) between PFOS-coated NPs and POPC membrane in pure water and 0.1 M KCl solution. The interaction energies in the final 20 ns are averaged

| Solution	E_{elect} (kJ mol^{-1})	E_{LJ} (kJ mol^{-1})
Pure water	-558.9 ± 177.2	-226.8 ± 36.2
0.1 M KCl	-628.3 ± 274.5	-159.7 ± 79.2

attaching to the PFOA–NP complex (Fig. S9). The configuration shows that more PFOA molecules detach from the NP surface compared with the PFOS-coated NP system. Specifically, 11 out of 40 PFOA molecules detach from the NP and diffuse into the solution or even insert into the lipid membrane over 250 ns (Fig. S10 and Table S1 in the SI), while for the case of the PFOS-coated NP, there are only 3 PFOS molecules detached from the NP surface after 240 ns. As shown in Fig. S11 in the SI, both the POPC surface and the POPC lipid surface exhibit attraction to the PFOA molecules. The competing interactions lead to the instability of the PFOA molecules on the NP surface. Similar to the case of the PFOS-coated NP, when the PFOA-coated NP adsorbs onto POPC, the negatively charged $-CO_2^-$ groups of PFOA interact electrostatically with the positively charged $-N^+(CH_3)_3$ groups of POPC, facilitating adsorption. However, as PFOA molecules detach, parts of the NP surface become exposed, and the PFOA-coated NP rotates on the POPC membrane. As shown in Fig. 9, once exposed, the interactions between the POPC bilayer and the PFOA–NP complex weaken when the uncharged NP region faces the POPC surface, ultimately leading to desorption of the PFOA–NP complex.

In the 0.1 M KCl solution, a similar number of PFOA molecules detach from the NP surface, resulting in comparable adsorption–desorption behavior on the POPC membrane surface (Fig. S12 in the SI). The difference in adsorption stability between PFOA and PFOS on the NP surface can be attributed to the charge densities of their polar headgroups. Because PFOA has a higher charge density than PFOS,[80] the electrostatic repulsion between the adsorbed PFOA molecules is stronger than that among PFOS molecules, leading to more PFOA

molecules detaching from the NP surface and weaker interactions of PFOA-coated NP with the POPC membrane surface. Consistently, previous atomistic MD simulations[71] also showed that PFOS can adsorb on the graphene surface more strongly than PFOA. Our study underscores the role of anionic PFOA and PFOS attachment to the PS NP surface in enhancing PS NP interactions. This finding aligns with previous CG MD studies[81] showing that the formation of a lipid corona increases PS NP interactions with the bacterial extracellular polymeric substance (EPS) membrane.

Influence of PFOS-NP adsorption on the lipid layer structure

To examine the impact of the adsorption of PFOS-coated NP on the POPC lipid membrane, the order parameter (S_{CH})[41] was
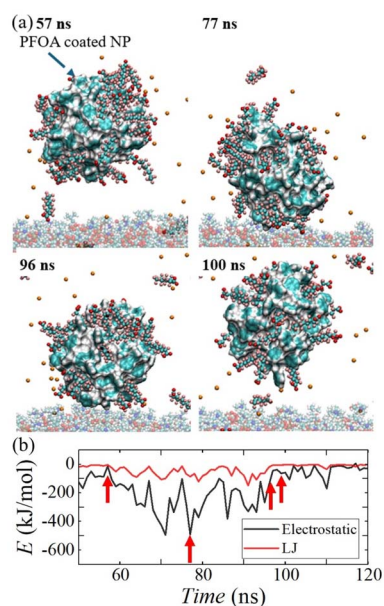
Fig. 9 (a) Snapshots of the rotation of a PFOA-coated NP on the POPC membrane over time and (b) corresponding energy (LJ and electrostatic) evolution. The arrows in (b) indicate the time for those snapshots in (a).
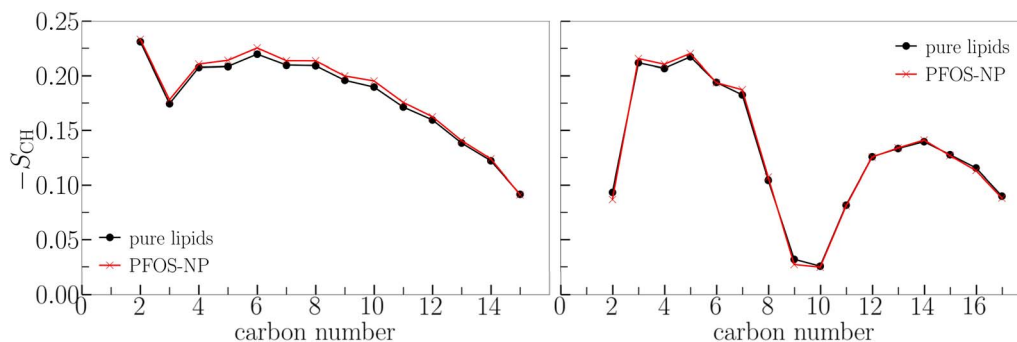
Fig. 10 Order parameter S_{CH} profiles of saturated sn-1 (left) and unsaturated sn-2 chains of POPC membranes (right) in different systems.

calculated for the saturated (sn-1) and unsaturated (sn-2) acyl chain tails of POPC lipids (Fig. 10). S_{CH} describes the orientation of C–H bond vectors relative to the bilayer normal (Z-axis), averaged over all lipids and sampling time,[41]

$$S_{CH} = \frac{\langle 3\cos^2\theta - 1 \rangle}{2} \qquad (3)$$

where θ is an angle between the C–H bond vector and the normal direction of the lipid bilayer surface. Fig. 10 shows a slight difference in the S_{CH} profiles between the pure lipid membrane surface and the surface adsorbed with the PFOS-coated NP. The PFOS-coated NP attaches to the top polar groups of the lipid, which has only a minor effect on the structure of the acyl chains. In addition, as shown in our previous study,[41] the insertion of PFOA molecules can slightly enhance the ordering of the acyl chains. This effect offsets the small disorder induced by the adsorption of the PFOS-coated NP.

The surface diffusion coefficient (D) of different POPC groups on the X–Y plane, excluding hydrogen atoms, to characterize the influence of PFOS-coated NP adsorption on lipid mobility using Einstein's relation.[82,83] A slight increase in D is observed for the surface-exposed zwitterionic phosphocholine group: 1.03×10^{-7} cm^2 s^{-1} for pure lipid bilayer and 1.45×10^{-7} cm^2 s^{-1} for the bilayer with an adsorbed PFOS-coated NP and the insertion of three PFOS molecules. Similar small increases in D are detected for the carbon atoms of the saturated (sn-1) and unsaturated (sn-2) acyl chain tails, from 1.10×10^{-7} cm^2 s^{-1} for pure lipid bilayer to 1.67×10^{-7} cm^2 s^{-1} after PFOS-coated NP adsorption.

Conclusions

The co-existence of PFAS and nanoplastics (or microplastics) poses a combined potential threat to both the environment and human health. In this study, we investigated the formation of PFAS–polystyrene NP complexes and the interfacial behavior of PFAS-NP on the zwitterionic POPC lipid bilayer surfaces using atomistic MD simulations. Different PFAS molecules were examined, including charge-neutral PTFE and the two anionic species (PFOS and PFOA). Our simulations demonstrate that the PS-NPs can serve as PFAS carriers to transfer PFAS molecules from bulk water to the lipid membrane surface. The attachment

of PFAS molecules on the PS-NP surface also alters the interfacial behavior of NPs at the lipid/water interface.

Our simulations show that charge-neutral PTFE and anionic PFAS compounds (PFOS and PFOA) strongly adsorb onto the PS NP surfaces. PFAS adsorption on NPs is primarily driven by hydrophobic and fluorophilic interactions. However, distinct adsorption behaviors are observed between the anionic species (PFOA and PFOS) and neutral PTFE. The anionic molecules form homogeneous, equilibrated adsorption layers due to electrostatic repulsion among their negatively charged carboxylate or sulfonate groups. In contrast, neutral PTFE exhibits inhomogeneous adsorption characterized by nonequilibrated segregation and deep penetration into the NP surface. PFOA and PFOS preferentially lie flat on the NP surface or adopt a stand-up orientation, with their charged headgroups exposed to water and fluorocarbon chains oriented toward the NP core. Neutral PTFE molecules also adsorb onto the NP surface; in the larger NPs (6.7 nm), they penetrate slightly into the core, whereas in the smaller NPs, they aggregate within the NP interior.

Our study shows that in the zwitterionic POPC lipid membrane, more positively charged trimethylammonium groups interact with non–hydrogen-bonded water and are exposed at the surface than the underlying negatively charged phosphate groups that form hydrogen bonds with water. This surface structure limits the membrane's resistance to NP adsorption. Although the highly hydrated POPC surface hinders attachment of charge-neutral bare NPs (3.1–6.7 nm) or PTFE-coated NPs, anionic PFOS-coated NPs rapidly adsorb due to electrostatic attraction to the positively charged choline groups, overcoming the hydration barrier. PFOA-coated NPs also attach but exhibit unstable adsorption; more PFOA molecules detach from the PS-NP surface than PFOS, exposing the NP core and weakening NP–lipid interactions, which leads to NP desorption. In the meantime, those detached PFOS and PFOA molecules rapidly insert into the POPC lipids. Changing the aqueous environment from pure water to a 0.1 M KCl solution does not result in any noticeable change in the interfacial behavior of small PFAS–NP complexes with the diameters of around 3.1 nm.

It is worth noting that, in environmental settings, NPs can possess diverse chemical additives and surface chemistries, such as amino-modified PS-NPs and PS-carboxylated NPs.[84] *In*

vivo, cell membranes also contain additional components such as cholesterol, which can influence NP–membrane interactions. These factors will be investigated in future work. We will also further examine the effects of ionic strength and NP size on surface binding. The behavior of PFAS-coated nanoparticles will likewise be explored using the potential of free energy profile. Nevertheless, our study provides valuable molecular-level insights into the mechanisms governing PFAS–NP colloidal transport and their potential pathological effects. These findings are also crucial for the development of water purification technologies aimed at removing such toxic compounds.

It is also notable that, in real environmental conditions, the surface chemistry and composition of PS NPs are complex due to their aging effects and interactions with the surrounding environment. These factors can alter the interactions between PFAS and lipid membranes. The current work focuses only on an idealized model and does not consider these complex effects. More detailed investigations of more realistic PS NP from the environment will be performed in future studies.

Author contributions

Jiahuiyu Fang: conceptualization, investigation (interactions of PFAS-coated NPs with lipids), formal analysis (interactions of PFAS-coated NPs with lipids), methodology, validation, visualization, data curation, and writing–original draft. Tongxuan Qiao: conceptualization, investigation (formation of PFAS–NP complex), formal analysis (formation of PFAS–NP complex), methodology, validation, visualization, data curation, and writing–original draft (interactions of PFAS-coated NPs with lipids). Pranab Sarker: formal analysis (formation of PFAS–NP complex), methodology, validation, visualization, and writing–original draft. Xiaoxue Qin: formal analysis (formation of PFAS–NP complex), methodology, validation, visualization, and writing–original draft. Size Zheng: formal analysis (formation of PFAS–NP complex), methodology, validation, visualization, and writing–original draft. Mark J. Uline: conceptualization, investigation, validation, project administration, resources, supervision, and writing–review & editing. Tao Wei: conceptualization, investigation, formal analysis, methodology, validation, visualization, data curation, project administration, resources, funding acquisition, supervision, and writing–review & editing.

Conflicts of interest

There are no conflicts to declare.

Data availability

The authors confirm that the data supporting the findings of this study is available within the article and its supplementary information (SI). Supplementary information is available. See DOI: https://doi.org/10.1039/d5na01071c.

Acknowledgements

References

1 R. C. Buck, J. Franklin, U. Berger, J. M. Conder, I. T. Cousins, P. De Voogt, A. A. Jensen, K. Kannan, S. A. Mabury and S. P. Van Leeuwen, *Integr. Environ. Assess. Manage.*, 2011, **7**, 513–541.

2 A. B. Lindstrom, M. J. Strynar and E. L. Libelo, *Environ. Sci. Technol.*, 2011, **45**, 7954–7961.

3 J. Glüge, M. Scheringer, I. T. Cousins, J. C. DeWitt, G. Goldenman, D. Herzke, R. Lohmann, C. A. Ng, X. Trier and Z. Wang, *Environ. Sci. Process. Impacts*, 2020, **22**, 2345–2373.

4 M. R. Winburn, M. F. Alvarado and C. L. Cheung, *Nanoscale*, 2025, **17**, 2138–2146.

5 A. F. Prada, J. W. Scott, L. Green and T. J. Hoellein, *Sci. Total Environ.*, 2024, **954**, 176751.

6 L. Ahrens, M. Shoeib, T. Harner, S. C. Lee, R. Guo and E. J. Reiner, *Environ. Sci. Technol.*, 2011, **45**, 8098–8105.

7 H. Hamid, L. Y. Li and J. R. Grace, *Environ. Pollut.*, 2018, **235**, 74–84.

8 J. W. Scott, K. G. Gunderson, L. A. Green, R. R. Rediske and A. D. Steinman, *Toxics*, 2021, **9**, 106.

9 P. Casal, B. González-Gaya, Y. Zhang, A. J. Reardon, J. W. Martin, B. Jiménez and J. Dachs, *Environ. Sci. Technol.*, 2017, **51**, 2766–2775.

10 Y. Fujii, Y. Kato, K. Sakamoto, T. Matsuishi, K. H. Harada, A. Koizumi, O. Kimura, T. Endo and K. Haraguchi, *Sci. Total Environ.*, 2018, **616**, 554–563.

11 M. Smithwick, R. J. Norstrom, S. A. Mabury, K. Solomon, T. J. Evans, I. Stirling, M. K. Taylor and D. C. Muir, *Environ. Sci. Technol.*, 2006, **40**, 1139–1143.

12 A. A. Shah, F. Hasan, A. Hameed and S. Ahmed, *Biotechnol. Adv.*, 2008, **26**, 246–265.

13 J. C. DeWitt, *Toxicological Effects of Perfluoroalkyl and Polyfluoroalkyl Substances*, Springer International Publishing, Cham, 2015.

14 J. M. Liddie, L. A. Schaider and E. M. Sunderland, *Environ. Sci. Technol.*, 2023, **57**, 7902–7912.

15 N. P. Ivleva, *Chem. Rev.*, 2021, **121**, 11886–11936.

16 R. C. Thompson, Y. Olsen, R. P. Mitchell, A. Davis, S. J. Rowland, A. W. John, D. McGonigle and A. E. Russell, *Science*, 2004, **304**, 838.

17 S. M. Meppelink, D. W. Kolpin, G. H. LeFevre, D. M. Cwiertny, C. E. Givens, L. A. Green, L. E. Hubbard, L. R. Iwanowicz, R. F. Lane and A. L. Mianecki, *Environ. Sci. Process. Impacts*, 2025, **27**, 1401–1422.

18 P. L. Corcoran, in *Handbook of Microplastics in the Environment*, Springer, 2022, pp. 531–542.

19 J. P. McDevitt, C. S. Criddle, M. Morse, R. C. Hale, C. B. Bott and C. M. Rochman, *Environ. Sci. Technol.*, 2017, **51**, 6611–6617.

20 G. S. Ustabasi and A. Baysal, *Environ. Monit. Assess.*, 2019, **191**, 438.

21 Y. Chae and Y.-J. An, *Mar. Pollut. Bull.*, 2017, **124**, 624–632.

22 X. Liu, W. Wei, Z. Chen, L. Wu, H. Duan, M. Zheng, D. Wang and B.-J. Ni, *Nat. Water*, 2025, **3**, 764–781.

23 Z. Yu, X. Fan, X. Zhao, T. He, X. Li, H. Du, M. Zhao, R. Zhu, M. Li and Z. Zhang, *ACS Appl. Mater. Interfaces*, 2024, **16**, 34524–34537.

24 S. O. Fakayode, T. F. Mehari, V. E. Fernand Narcisse, C. Grant, M. E. Taylor, G. A. Baker, N. Siraj, M. Bashiru, I. Denmark and A. Oyebade, *Appl. Spectrosc. Rev.*, 2024, **59**, 1183–1277.

25 X. Hua and D. Wang, *Rev. Environ. Contam. Toxicol.*, 2022, **260**, 12.

26 L. Liu, K. Xu, B. Zhang, Y. Ye, Q. Zhang and W. Jiang, *Sci. Total Environ.*, 2021, **779**, 146523.

27 X. Lin and X. Lin, *Nanoscale*, 2021, **13**, 9825–9833.

28 A. Khan and Z. Jia, *Iscience*, 2023, **26**, 106061.

29 L. Wang, W.-M. Wu, N. S. Bolan, D. C. Tsang, Y. Li, M. Qin and D. Hou, *J. Hazard. Mater.*, 2021, **401**, 123415.

30 W. S. Lee, H.-J. Cho, E. Kim, Y. H. Huh, H.-J. Kim, B. Kim, T. Kang, J.-S. Lee and J. Jeong, *Nanoscale*, 2019, **11**, 3173–3185.

31 O. A. Salawu, C. I. Olivares and A. S. Adeleye, *J. Hazard. Mater.*, 2024, **470**, 134185.

32 N. Parashar, B. Mahanty and S. Hait, *Water Emerging Contam. Nanoplast.*, 2023, **2**, 15.

33 F. Yu, J. Wu, H. Wang, Y. Bao, H. Xing, W. Ye, X. Li and M. Huang, *Sci. Total Environ.*, 2024, **948**, 175000.

34 W. Xie, J. Wang, Z. Song, Y. Chen and X. Lyu, *Water, Air, Soil Pollut.*, 2025, **236**, 936.

35 F. Wang, K. M. Shih and X. Y. Li, *Chemosphere*, 2015, **119**, 841–847.

36 Y. Cheng, L. Mai, X. Lu, Z. Li, Y. Guo, D. Chen and F. Wang, *Environ. Pollut.*, 2021, **281**, 117025.

37 Y. Wang, S. B. Darling and J. Chen, *ACS Appl. Mater. Interfaces*, 2021, **13**, 60789–60814.

38 A. M. Elgarahy, A. Akhdhar and K. Z. Elwakeel, *J. Environ. Chem. Eng.*, 2021, **9**, 106224.

39 T. Soltanighias, A. Umar, M. Abdullahi, M. A.-E. Abdallah and L. Orsini, *Environ. Pollut.*, 2024, **363**, 125133.

40 Y. Dai, J. Zhao, C. Sun, D. Li, X. Liu, Z. Wang, T. Yue and B. Xing, *Front. Environ. Sci. Eng.*, 2022, **16**, 136.

41 S. Zheng, P. Sarker, D. Gursoy, T. Wei and B. S. Hsiao, *Langmuir*, 2025, **41**, 9369–9376.

42 C. M. Luft, T. C. Schutt and M. K. Shukla, *Environ. Sci. Technol.*, 2022, **56**, 10053–10061.

43 Z. A. Gandhi, T. Lu, W. Guo, R. Crisci, J. Gao, M. C. Wilson, C. R. So, P. Sarker, X. Qin, T. Wei and Z. Chen, *J. Phys. Chem. Lett.*, 2025, **16**, 4031–4037.

44 W. Guo, T. Lu, R. Crisci, S. Nagao, T. Wei and Z. Chen, *Chem. Sci.*, 2023, **14**, 2999–3009.

45 T. Wei, H. Ma and A. Nakano, *J. Phys. Chem. Lett.*, 2016, **7**, 929–936.

46 Q. Fu, S. Zheng, N. Verma, R. Gambarini, T. Wei, B. M. Ocko and B. S. Hsiao, *Macromol.*, 2024, **58**, 723–732.

47 Y. Wu, T. Lin, E. Santos, D. Ahn, R. Marson, P. Sarker, X. Chen, F. Gubbels, N. E. Shephard, C. Mohler, T. Wei, T.-C. Kuo and Z. Chen, *Soft Matter*, 2024, **20**, 4765–4775.

48 J. Chen, E. Xu, Y. Wei, M. Chen, T. Wei and S. Zheng, *Langmuir*, 2022, **38**, 10817–10825.

49 S. Zheng, Y. Wei, Y. Lin and T. Wei, *Appl. Phys. Lett.*, 2023, **122**, 253701.

50 A. D. Duraes, E. L. Jiao and W. Zhang, *J. Phys. Chem. B*, 2025, **129**, 3385–3395.

51 G. Łazarski, N. Rajtar, M. Romek, D. Jamróz, M. Rawski and M. Kepczynski, *J. Phys. Chem. B*, 2025, **129**, 4110–4122.

52 D. Sil, E. Osmanbasic, S. C. Mandal, A. Acharya and C. Dutta, *J. Phys. Chem. Lett.*, 2024, **15**, 5428–5435.

53 M. Zhang, B. Ren, Y. Liu, G. Liang, Y. Sun, L. Xu and J. Zheng, *ACS Chem. Neurosci.*, 2017, **8**, 1789–1800.

54 Y. Liu, D. Zhang, Y. Zhang, Y. Tang, L. Xu, H. He, J. Wu and J. Zheng, *J. Phys. Chem. B*, 2020, **124**, 7830–7841.

55 J. Fang, P. Sarker, X. Qin, S. Zhang, S. Zheng and T. Wei, *Nanoscale*, 2025, **17**, 16737–16747.

56 A. Choubey, M. Vedadi, K.-i. Nomura, R. K. Kalia, A. Nakano and P. Vashishta, *Appl. Phys. Lett.*, 2011, **98**, 023701.

57 X. Lin and X. Lin, *Biomater. Sci.*, 2021, **9**, 8249–8258.

58 G. Hu, B. Jiao, X. Shi, R. P. Valle, Q. Fan and Y. Y. Zuo, *ACS Nano*, 2013, **7**, 10525–10533.

59 Y. Xu, S. Li, Z. Luo, H. Ren, X. Zhang, F. Huang, Y. Y. Zuo and T. Yue, *Langmuir*, 2018, **34**, 9054–9063.

60 L. Li, Y. Xu, S. Li, X. Zhang, H. Feng, Y. Dai, J. Zhao and T. Yue, *J. Hazard. Mater.*, 2022, **427**, 127872.

61 Z. Shen, J. Ge, H. Ye, S. Tang and Y. Li, *J. Phys. Chem. B*, 2020, **124**, 5415–5425.

62 Q. Wang, R. Xu, F. Zha, L. Xu, B. Kang and H. Han, *Comput. Geotech.*, 2025, **187**, 107461.

63 M. J. Abraham, T. Murtola, R. Schulz, S. Páll, J. C. Smith, B. Hess and E. Lindahl, *SoftwareX*, 2015, **1**, 19–25.

64 J. Huang and A. D. MacKerell Jr, *J. Comput. Chem.*, 2013, **34**, 2135–2145.

65 A. D. MacKerell Jr, D. Bashford, M. Bellott, R. L. Dunbrack Jr, J. D. Evanseck, M. J. Field, S. Fischer, J. Gao, H. Guo and S. Ha, *J. Phys. Chem. B*, 1998, **102**, 3586–3616.

66 S. Miyamoto and P. A. Kollman, *J. Comput. Chem.*, 1992, **13**, 952–962.

67 G. F. von Rudorff, T. Watermann and D. Sebastiani, *J. Phys. Chem. B*, 2014, **118**, 12531–12540.

68 S. Jo, T. Kim, V. G. Iyer and W. Im, *J. Comput. Chem.*, 2008, **29**, 1859–1865.

69 M. Parrinello and A. Rahman, *J. Appl. Phys.*, 1981, **52**, 7182–7190.

70 A. Román Santiago, S. Yin, J. Elbert, J. Lee, D. Shukla and X. Su, *J. Am. Chem. Soc.*, 2023, **145**, 9508–9519.

71 B. G. Lamb and B. Ma, *Nanoscale*, 2025, **17**, 10632–10643.

72 B. Qiao, F. Jiménez-Ángeles, T. D. Nguyen and M. Olvera de la Cruz, *Proc. Natl. Acad. Sci. U. S. A.*, 2019, **116**, 19274–19281.

73 X. Qin, A. A. Chen, J. Fang, P. Sarker, M. J. Uline and T. Wei, *Langmuir*, 2024, **40**, 23994–24001.

74 P. Sarker, G. T. Chen, M. S. J. Sajib, N. W. Jones and T. Wei, *Colloids Surf. A Physicochem. Eng. Asp.*, 2022, **653**, 129943.

75 S. Zheng, J. Gissinger, B. S. Hsiao and T. Wei, *ACS Appl. Mater. Interfaces*, 2024, **16**, 65677–65686.

76 H. Huang, C. Zhang, R. Crisci, T. Lu, H.-C. Hung, M. S. J. Sajib, P. Sarker, J. Ma, T. Wei and S. Jiang, *J. Am. Chem. Soc.*, 2021, **143**, 16786–16795.

77 G. Łazarski, N. Rajtar, M. Romek, D. Jamróz, M. Rawski and M. Kepczynski, *J. Phys. Chem. B*, 2025, **129**, 4110–4122.

78 A. A. Gurtovenko, *Langmuir*, 2025, **41**, 25187–25196.

79 L. Li, S. Li, Y. Xu, L. Ren, L. Yang, X. Liu, Y. Dai, J. Zhao and T. Yue, *Environ. Sci. Nano*, 2023, **10**, 440–453.

80 F. Dixit, B. Barbeau, S. G. Mostafavi and M. Mohseni, *Environ. Sci.: Water Res. Technol.*, 2019, **5**, 1782–1795.

81 Y. Liu, T. Yue, L. Liu, B. Zhang, H. Feng, S. Li, X. Liu, Y. Dai and J. Zhao, *J. Hazard. Mater.*, 2023, **457**, 131825.

82 T. Wei, T. Huang, B. Qiao, M. Zhang, H. Ma and L. Zhang, *J. Phys. Chem. B*, 2014, **118**, 13202–13209.

83 C. M. Nakano, H. Ma and T. Wei, *Appl. Phys. Lett.*, 2015, **106**, 153701.

84 D. Xu, Y. Ma, X. Han and Y. Chen, *J. Hazard. Mater.*, 2021, **417**, 126092.